



Cite this: *RSC Adv.*, 2024, 14, 20390

# Excellent mechanical and electromagnetic interference shielding properties of polylactic acid/polycaprolactone/multiwalled carbon nanotube composites enabled by a multilayer structure design

Xiaocheng Li,<sup>a</sup> Bingbing Zeng,<sup>c</sup> Yu Zheng <sup>\*c</sup> and Jintang Zhou<sup>\*ab</sup>

In this work, a special multilayer structure consisting of polylactic acid (PLA) and a co-continuous PLA/polycaprolactone (PCL)/multiwalled carbon nanotube (MWCNT) (ALM) composite with a double-percolated conductive network was fabricated via layer-assembly coextrusion. It was revealed that PLA domains located at the layer interface could serve as rivets properly linking adjacent layers. Such a nacre-like structure with alternately stacked rigid PLA and flexible ALM increased the fracture strain to 354.4%, nearly quadruple that of the PLA/PCL/MWCNT conventional blending composite with the same composition, while maintaining an excellent strength above 46.0 MPa. In addition, the multilayer composites showed a special frequency-selective electromagnetic interference (EMI) shielding performance, with tunable shielding peak positions controlled by the layer number. Their maximum EMI shielding effectiveness almost contributed by absorption loss could reach 49.8 dB, which originated from two aspects: one was the high electrical conductivity offered by the double-percolated distribution of MWCNTs, and the other was the multiple wave attenuation effect that occurred at the interfaces between PLA and ALM layers and the blend interfaces in ALM layers. This effort paves a new way for developing composites with outstanding mechanical and EMI shielding properties that can be extended to other polymeric composite systems.

Received 31st March 2024

Accepted 13th June 2024

DOI: 10.1039/d4ra02440k

rsc.li/rsc-advances

## 1 Introduction

Biodegradable polylactic acid (PLA) is undoubtedly one of the most important bioplastics worldwide and is greatly expected to be a sustainable substitute for fossil-based polymers.<sup>1–3</sup> Despite its numerous advantages, such as great transparency, high strength, high modulus, and good processability, the inherent brittleness of PLA severely limits its wide applications.<sup>4,5</sup> Hence, the quest to fabricate tough PLA has remained the focus of attention in both academia and industry. Recently, with the rapid development of science and technology, the requirements for the practical application of PLA are not only limited to stable mechanical performance, but have also extended to the

realization of extra functionality, such as electrical conduction and electromagnetic interference (EMI) shielding.<sup>6–8</sup>

With a focus on sustainable development, many efforts have been undertaken to modify PLA's mechanical properties by blending it with soft biodegradable polyesters, such as poly(butylene adipate-co-terephthalate) (PBAT),<sup>9</sup> poly(butylene succinate) (PBS),<sup>10</sup> and polycaprolactone (PCL).<sup>11</sup> Among them, flexible PCL has been commonly used to alter the PLA nature from rigid to ductile owing to their perfect complementarity. Nevertheless, the enhancement in the ductility of PLA/PCL blend is generally accompanied with the deterioration of strength. For example, Peponi *et al.*<sup>12</sup> explored the effect of PCL content on the mechanical properties of PLA/PCL blend and found that the sample with 30 wt% PCL presented the best overall performance: elongation at break reached around 200%, but tensile strength decreased to 32 MPa, which is much less than that of pristine PLA (~70 MPa). An efficient approach to address this issue is incorporating reinforcing fillers into PLA/PCL blend.<sup>13–15</sup> For instance, Suman *et al.*<sup>13</sup> attempted to enhance the mechanical properties of PLA/PCL (80/20) blend using montmorillonite nanoclay. It was found that the addition of 4% nanoclay to the blend resulted in an improvement in tensile strength and modulus by approximately 15% and 26%,

<sup>a</sup>College of Materials Science and Technology, Nanjing University of Aeronautics and Astronautics, Nanjing 211100, China. E-mail: imzjt@126.com

<sup>b</sup>Key Laboratory of Material Preparation and Protection for Harsh Environment (Nanjing University of Aeronautics and Astronautics), Ministry of Industry and Information Technology, Nanjing 211100, China

<sup>c</sup>The State Key Laboratory of Polymer Materials Engineering, Polymer Research Institute of Sichuan University, Chengdu 610065, Sichuan, China. E-mail: zy1990@scu.edu.cn



respectively, as compared to the blend. Unfortunately, these works focused only on the optimization of mechanical performance but not on the synchronous creation of extra functions.

The multiwalled carbon nanotube (MWCNT) merges high strength, good toughness, and superior electrical conduction, which have been widely used to develop polymeric composites with excellent mechanical properties and electrical functions.<sup>16</sup> Thus far, some studies have been conducted to explore the effect of MWCNT addition on the structural, mechanical, and electrical properties of PLA/PCL blend. For example, it was revealed that MWCNTs are selectively dispersed in PCL regardless of the PCL domain size and the mixing order of PLA, PCL, and MWCNT.<sup>17,18</sup> Therefore, aiming at achieving high electrical conductivity and EMI shielding effectiveness (SE), the PCL phase in PLA/PCL/MWCNT (ALM) composite is desired to be continuous for constructing the double-percolated conductive network, where the MWCNTs confined in PCL can be densely connected.<sup>19,20</sup> This double percolation effect usually occurs in the presence of a higher PCL content (40–60 wt%). Consequently, the reinforcing effect provided by MWCNT fails to offset the plasticization effect induced by the excessive addition of PCL.<sup>21</sup> The strength of the PLA/PCL (60/40) blend decreased to ~36 MPa even after incorporating with 3 wt% MWCNTs and accompanied by an over 50% decrease in fracture strain. Consequently, for the ALM composite, the challenge is how to balance the mechanical properties and electrical performance as well as EMI SE. This will undoubtedly lead to an artful morphology structure design combined with MWCNT distribution control.

In this work, morphological regulation was applied to develop PLA-based composites with outstanding mechanical properties and high EMI SE through the novel layer-assembly coextrusion technology.<sup>22–24</sup> As schematically shown in Fig. 1, the ALM composite pellets with a double-percolated conductive network were first prepared by melt blending and then coextruded with the pure PLA, forming a special co-continuous multilayer structure. The PLA domains in the co-continuous ALM layers can serve as rivets to link the PLA layers appropriately so that the nacre-like<sup>25,26</sup> PLA/ALM alternated stacking structure enables the maximum contribution to the stiffness and toughness, resulting in a tensile strength above 46.0 MPa and failure strain up to 354.4%. In addition, the high electrical conductivity originating from the double-percolated network endows the multilayer composites with an excellent EMI SE, which can be increased up to 49.8 dB because of the multiple wave attenuation effect occurring at the interfaces between the PLA and ALM layers and the blend interfaces in the individual ALM layers. This multilayer structure design concept can be extended to various combinations of polymeric composite systems. Thus, we believe that the present work paves the way for fabricating materials with multifunctionality.

## 2 Experimental

### 2.1 Materials

The commercial PCL CAPA 6800, with an average molecular weight of  $8.84 \times 10^5 \text{ g mol}^{-1}$  and a density of  $1.11 \text{ g cm}^{-3}$ , was

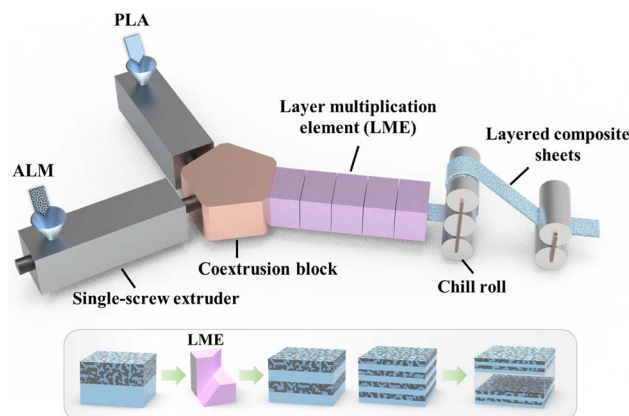


Fig. 1 Schematic of the layer-assembly coextrusion system.

purchased from Perstorp (Sweden). The extrusion-grade PLA 4032D, with an average molecular weight of  $2.23 \times 10^5 \text{ g mol}^{-1}$  and a density of  $1.24 \text{ g cm}^{-3}$ , was purchased from Nature Works (USA). The MWCNT NC 7000, with an average diameter of 9.5 nm and an average length of 1.5  $\mu\text{m}$ , was supplied by Nanocyl SA (Belgium).

### 2.2 Sample preparation

Before melt processing, PLA and MWCNT were dried overnight at 80 °C and PCL at 40 °C to prevent moisture-induced degradation. ALM composites with a mass ratio of 50/50/4 were prepared in a twin-screw extruder (screw diameter of 25 mm and  $L/D$  of 40, Nanjing Giant Co. Ltd, China) with a 150–180–185–175 °C temperature profile from the hopper to the die. Then, the alternating PLA/ALM multilayer sheets were prepared using the layer-assembly coextrusion setup, as schematically shown in Fig. 1. The two kinds of pellets were simultaneously put into separate single-screw extruders with a 150–185–180 °C temperature profile. Initially, the PLA and ALM melts were vertically arranged into a bilayer arrangement in the coextrusion block. The thickness ratio of the PLA and ALM layers was fixed at 50 : 50 by controlling the feed rate of each melt using the gear pumps located between the extruder and the coextrusion block; thus, the mass ratio of PLA/PCL/MWCNT in the whole composite was around 75/25/2 wt%. Then, the bilayer melt went through a series of layer-multiplying elements (LME) at 180 °C to achieve layer multiplication. In an LME, the melt is vertically split into two parts in the middle, and each part is subsequently compressed and stretched back to the original width with half thickness and finally restacked with the layer number doubled. The final layer number should be  $2^{(n+1)}$  if the number of LMEs was  $n$ . In this work, the PLA/ALM multilayer sheets with layer numbers ranging from 4 to 64 were fabricated, which were sequentially named as 4L, 8L, etc. The layer number no longer increased after reaching 64 because the layer structure breakup occurred with the addition of one LME. For comparison, the PLA/PCL/MWCNT conventional blending composite (CBC) sheet with the same composition was prepared using only one extruder to maintain a similar



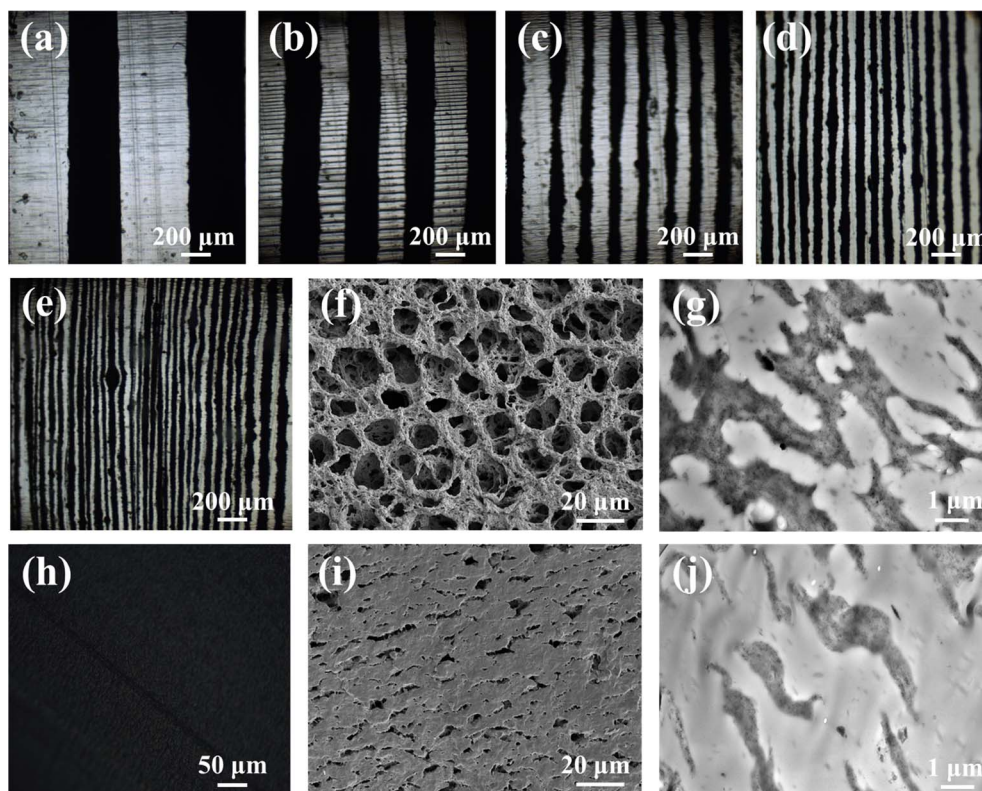


Fig. 2 (a–e) PLM images of the PLA/ALM multilayer composites; (f and g) SEM and TEM images of the individual ALM layer; and (h–j) PLM, SEM, and TEM images of CBC.

processing history. The thickness of each extrudate was maintained at 1.6 mm.

### 2.3 Morphological structure and MWCNT distribution

An approximately 10  $\mu\text{m}$  thick slice was cut from the sample using a microtome. Then, a polarizing light microscope (PLM, BX51, OLYMPUS) was used to observe the morphology structure directly. Subsequently, the morphology of the composites was further observed using a field-emission scanning electron microscope (SEM, JEOL JSM-5900LV). Specimens were first cryofractured in liquid nitrogen and then immersed in methylbenzene at room temperature for 1.5 h to etch the PCL

selectively. The visualization was conducted after coating a golden layer on the fractured surface. Then, the MWCNT distribution was revealed using a transmission electron microscope (TEM, JEM-2010) under an appropriate accelerating voltage. Ultrathin slices with a thickness of 100 nm were cut from the samples using a diamond knife by cryo-ultramicrotomy (Leica EM FC6, Germany) at  $-100\text{ }^{\circ}\text{C}$ .

### 2.4 Differential scanning calorimetry (DSC)

Before DSC testing, overnight drying was applied to each sample at  $60\text{ }^{\circ}\text{C}$  to prevent the influence of moisture evaporation. DSC analysis was performed using DSC Q20 (TA

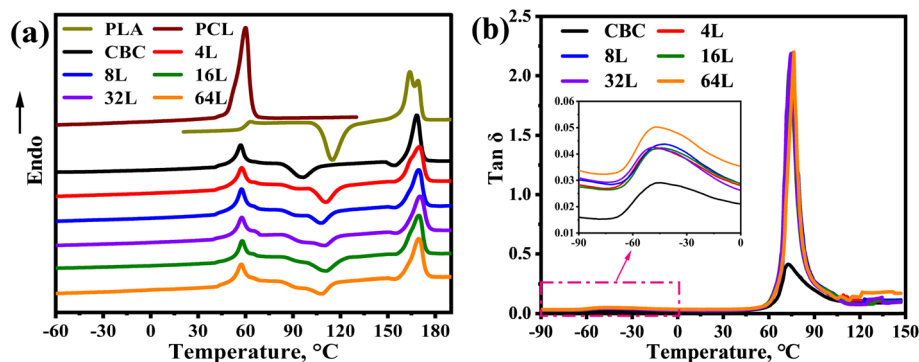


Fig. 3 (a) DSC heating curves of PCL, PLA and each composite, and (b)  $\tan \delta$  curves of each composite.





Table 1  $X_c$  and  $T_g$  of PCL and PLA

Sample	PCL	PLA	CBC	4L	8L	16L	32L	64L
$X_c$ of PCL, %	44.8	—	34.7	33.6	34.1	34.2	35.1	34.9
$X_c$ of PLA, %	—	3.5	9.0	10.2	10.7	11.0	12.3	13.5
DSC $T_g$ of PCL, °C	Unable to detect the $T_g$ of PCL by DSC							
DSC $T_g$ of PLA, °C	—	60.0	Overlapped by the melting peak of PCL					
DMA $T_g$ of PCL, °C	−50.0	—	−51.4	−50.3	−48.5	−49.6	−51.2	−50.1
DMA $T_g$ of PLA, °C	—	75.0	73.5	74.5	74.6	74.8	75.4	76.5

Instruments) under nitrogen flow. 5–8 mg of each sample was placed in a small crucible and then heated at a rate of  $10^\circ\text{C min}^{-1}$  from  $-80$  to  $200^\circ\text{C}$ . The crystallinity ( $X_c$ ) of PLA and PCL is calculated using the following equation:

$$X_c = \frac{\Delta H_m - \Delta H_{cc}}{\Delta H_{m100}} \times \frac{1}{w} \times 100\%, \quad (1)$$

where  $w$  is the mass fraction of PLA or PCL. The equation involves the enthalpy values:  $\Delta H_m$  represents the enthalpy of melting,  $\Delta H_{cc}$  represents the enthalpy of cold crystallization (the  $\Delta H_{cc}$  of PCL is  $0\text{ J g}^{-1}$ ), and  $\Delta H_{m100}$  represents the

theoretical enthalpy for melting a 100% crystalline PLA ( $93.7\text{ J g}^{-1}$ ) or a 100% crystalline PCL ( $136.0\text{ J g}^{-1}$ ).<sup>27,28</sup>

## 2.5 Dynamic mechanical analysis (DMA)

A sample with dimensions of  $10\text{ mm}$  (length)  $\times$   $4\text{ mm}$  (width)  $\times$   $1\text{ mm}$  (thickness) was cut from the center of the coextruded film. The DMA measurements were carried out using a DMA Q800 (TA Instruments). Each sample was tested using stretch mode with a frequency of  $1\text{ Hz}$  and an amplitude of  $10\text{ }\mu\text{m}$  and heated from  $-80$  to  $150^\circ\text{C}$  at a ramp rate of  $3^\circ\text{C min}^{-1}$ .

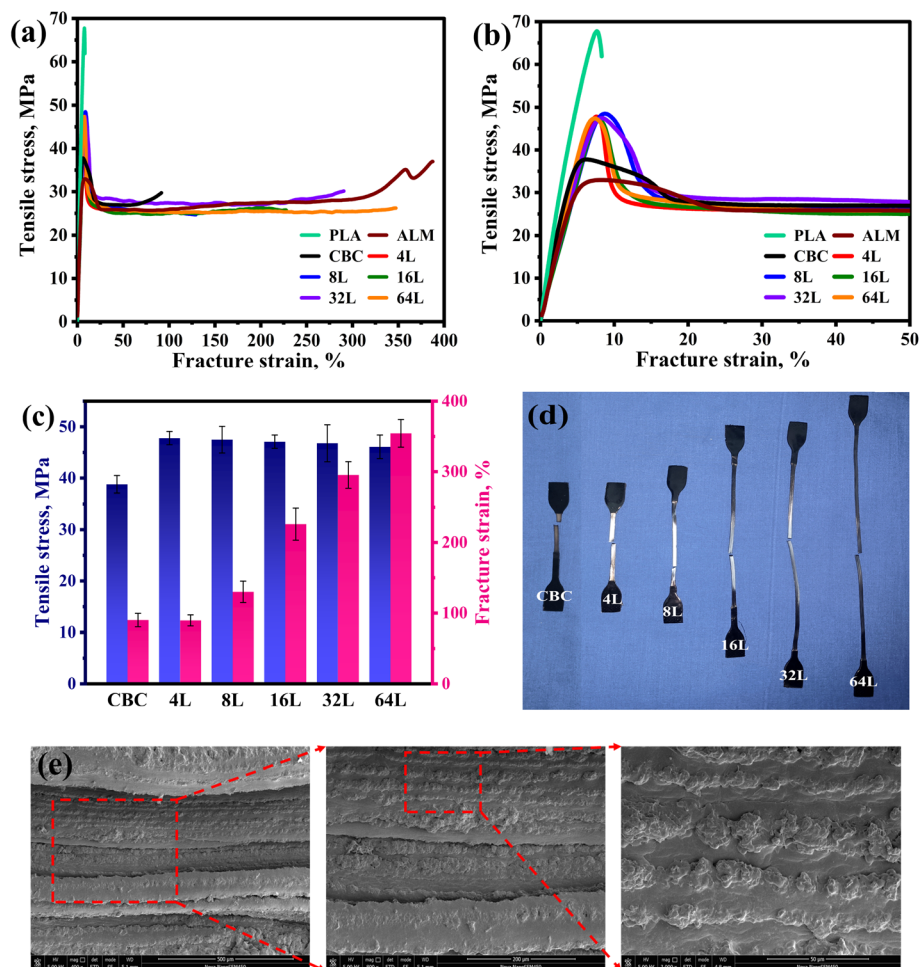


Fig. 4 (a and b) Stress–strain curves and their partial enlarged view, (c) tensile strength and fracture strain, and (d) pictures of the broken specimens of CBC and the multilayer composites; (e) SEM image of the broken 64L specimen.



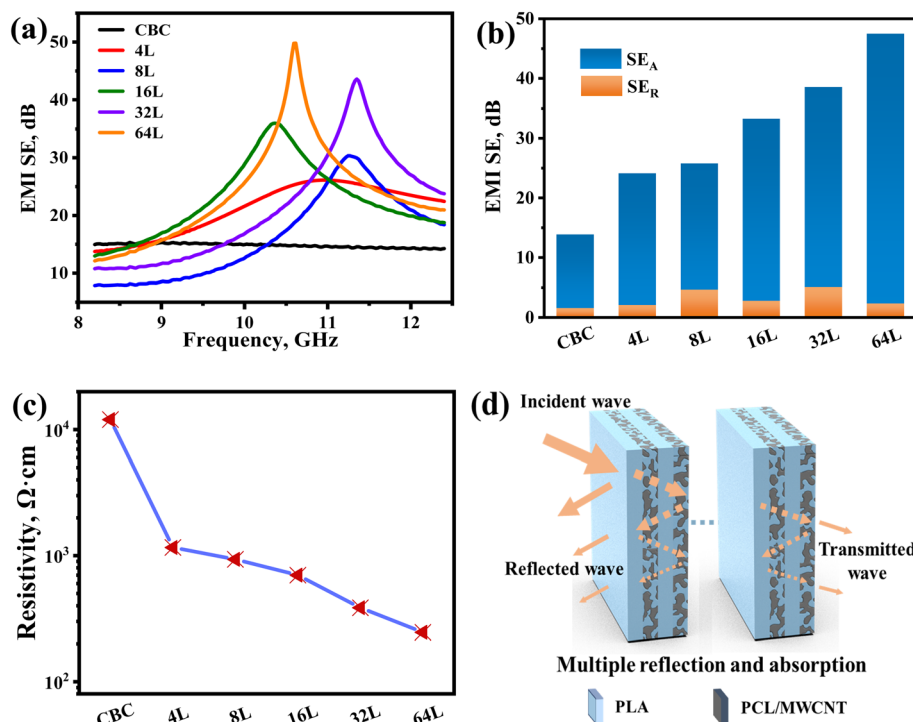


Fig. 5 (a) EMI SE of each composite in the X-Band. (b) SE<sub>A</sub> and SE<sub>R</sub>, and (c) electrical resistivity of each composite. (d) Schematic diagram of the EMI shielding mechanism of multilayer composites.

## 2.6 Electrical resistivity measurements

Rectangular splines with dimensions of 50.0 mm (length,  $L$ )  $\times$  10.0 mm (width,  $W$ )  $\times$  1.6 mm (thickness,  $T$ ) were cut from the samples for electrical resistivity testing. To avoid the influence of contact resistance, silver paste was coated on the spline edges. After the silver paste dried, the volume resistance ( $R$ ) of each spline was measured using a programmable insulation resistance tester (6487, Keithley Co. Ltd, USA) with an applied voltage of 1 V. The electrical resistivity ( $\rho$ ) was calculated using the following equation:<sup>29</sup>

$$\rho = R \frac{WT}{L}. \quad (2)$$

## 2.7 Mechanical property test

The dumbbell-shaped tensile specimens were cut from the coextruded films. The uniaxial tensile property of each specimen was tested on an Instron 4302 universal material testing machine (Norwood, MA, USA) with a tensile rate of 50 mm min<sup>-1</sup> in accordance with ASTM D638 standards. At least five specimens were tested for each composite.

## 2.8 EMI SE test

The EMI SE of the samples in the frequency range of 8.2–12.4 GHz (X-band) was measured using an Agilent N5247A vector network analyzer with an APC-7 connector. The testing samples with a diameter of 13.0 mm and a thickness of 1.6 mm were cut from the composites using a hollow punch. The output

parameters of forward reflection ( $S_{11}$ ), backward transmission ( $S_{12}$ ), forward transmission ( $S_{21}$ ), and backward reflection ( $S_{22}$ ) are applied to calculate the reflection coefficient ( $R$ ), transmission coefficient ( $T$ ), and absorption coefficient ( $A$ ) using eqn (3)–(5). Then, the reflection shielding effectiveness (SE<sub>R</sub>), absorption shielding effectiveness (SE<sub>A</sub>), and total electromagnetic shielding effectiveness (SE<sub>T</sub>) are calculated by applying eq. (6)–(8).<sup>30</sup> The SE<sub>M</sub> is the loss efficiency of multiple internal reflections, which can be ignored if SE<sub>T</sub> is larger than 10 dB.

$$R = |S_{11}|^2, \quad (3)$$

$$T = |S_{21}|^2, \quad (4)$$

$$A = 1 - R - T, \quad (5)$$

$$SE_R = -10 \lg(1 - R), \quad (6)$$

$$SE_A = -10 \lg\left(\frac{T}{1 - R}\right), \quad (7)$$

$$SE_T = SE_A + SE_R + SE_M. \quad (8)$$

# 3 Results and discussion

## 3.1 Morphological structures

The morphological structures of PLA/ALM multilayer composites were first characterized by PLM, as shown in Fig. 2a–e. The bright PLA and dark ALM were alternately assembled into

a regular multilayer structure. With the layer number multiplied, more layer interfaces were formed between PLA and ALM, while the single-layer thickness was proportionally decreased due to the invariant thickness of the whole composite. Obviously, the PLA domains located at the layer interface could serve as rivets to link the adjacent layers properly. Besides, the individual ALM exhibited a typical co-continuous structure as revealed by the SEM picture of ALM after etching PCL (Fig. 2f). Subsequently, TEM was applied to assess the MWCNT location in ALM. The TEM image in Fig. 2g shows that ALM has a co-continuous structure, and MWCNTs are selectively located in PCL (dark domains) rather than in PLA (bright domains), forming the double-percolated conductive network. Thus, coextruding PLA and ALM successfully tailored the low-content PCL (25 wt%) to be continuous, achieving a dense connection of MWCNTs. The morphology of CBC seems hard to characterize by PLM due to the disturbance of more uniformly distributed MWCNTs (Fig. 2h). The SEM image of CBC after etching PCL (Fig. 2i) presents a sea-island structure with the coexisting elongational and dispersed PCL phases, which was further evidenced by TEM observation, as shown in Fig. 2j. Moreover, the MWCNTs were selectively located in the PCL domains separated by the PLA matrix. Accordingly, a special co-continuous structural composite with a double-percolated conductive network was constructed *via* layer-assembly coextrusion.

### 3.2 Thermal behaviors

The DSC test was performed to investigate the thermal properties and crystallization behaviors of each composite, and the heating scans were recorded, as depicted in Fig. 3a. As can be observed, the pure PLA had a glass transition temperature ( $T_g$ ) at  $\sim 65$  °C and a strong cold crystallization ( $T_{cc}$ ) at  $\sim 115$  °C, followed by a double melting transition induced by the melt-recrystallization behavior.<sup>31</sup> In the thermogram of PCL, a sharp endothermic peak was found at  $\sim 60$  °C, corresponding to its melting temperature ( $T_m$ ). However, it seems unable to detect the  $T_g$  of PCL by DSC. After compounding PLA with PCL and MWCNT *via* simple blending or layer-assembly coextrusion, the  $T_g$  of PLA could not be detected due to the overlap of the glass transition of PLA and the melting peak of PCL. Therefore, the  $T_g$  of the composites was further evaluated by tracing the temperature where the maximum  $\tan \delta$  was located *via* DMA testing. As presented in Fig. 3b, all the composites exhibited two well-separated  $T_g$ s at  $\sim -50$  and  $75$  °C, implying that PLA and PCL have poor compatibility, regardless of the difference in phase morphology and MWCNT distribution among CBC and multilayer structures. The DSC results showed that the  $T_m$  values of PCL and PLA in the composites compared to the pure ones tended to be unchanged. However, in the composites, the cold crystallization of PLA began at a lower temperature, and the multiple melts of PLA vanished, suggesting that the addition of PCL and MWCNT promoted the PLA crystallization. The  $T_{CC}$  of multilayer composites was higher than that of CBC because the majority of PLA in layered composites existed as completely continuous solids and did not directly contact PCL

and MWCNT. Furthermore, the  $X_c$  of PCL and PLA in each composite was calculated, as listed in Table 1. The slight increase in  $X_c$  of PLA reinforced the view that the PLA crystallization is accelerated by PCL and MWCNT. Increasing the layer number increases this acceleration effect due to the newly formed layer interfaces, thus enhancing the contact between PLA and ALM. In contrast, all the composites exhibited a similar  $X_c$  of PCL ranging from 33.6% to 35.1%, which was smaller than that of pure PCL, indicating that the rigid PLA and MWCNT had a certain suppression effect on PCL crystallization. In summary, the thermal behaviors of multilayer composites resemble those of CBC, which could be ignored when discussing the effect of morphological distinction on their macroscopic properties.

### 3.3 Mechanical properties

The mechanical properties were studied by comparing the uniaxial tensile performance of multilayer composites with CBC. The typical stress-strain curves are shown in Fig. 4a (with a partially enlarged view in Fig. 4b), and the mechanical parameters of tensile strength ( $\sigma$ ) and fracture strain ( $\epsilon$ ) were obtained, as depicted in Fig. 4c. PLA showed a typical brittle tensile behavior with a high  $\sigma$  of  $\sim 70$  MPa but a poor  $\epsilon$  less than 10.0%. After incorporating the soft PCL and the rigid MWCNT, PLA was significantly toughened with  $\epsilon$  increased to 90.2% but  $\sigma$  dramatically decreased to 38.8 MPa. This means that the sea-island such as dispersion of PCL/MWCNT fails to simultaneously achieve high strength and high toughness. By tailoring CBC into a multilayer structure, the toughness and stiffness became more balanced. The composite with only 4 layers achieved a  $\sigma$  of 47.8 MPa enabled by the strength support from the completely continuous PLA layers and more densely connected MWCNTs, which had an  $\epsilon$  equivalent to that of CBC. Combined with the morphological characterization results in Fig. 2, some PLA domains in the ALM layers should be located at the layer interface due to the phase distribution feature of the co-continuous structure. This part of PLA acts as rivets to link the PLA and ALM layers properly, enabling the highly flexible ALM layer with an  $\epsilon$  of 387.6% to make the maximum contribution to the toughness. The numerous layer interfaces formed by multiplying the layer number amplified the riveting effect of the PLA in the interface area, leading to a significant increase in  $\epsilon$  but a slight decrease in  $\sigma$ . For the 64L specimen,  $\sigma$  was maintained at a high value of 46.1 MPa, while  $\epsilon$  was dramatically enhanced to 354.4%, nearly quadrupling that of CBC, which can be further evidenced by the photograph of the broken specimens in Fig. 4d. No layer debonding was found in the SEM picture of the 64L specimen after breaking (Fig. 4e), thereby showing excellent interfacial adhesion between the PLA and ATL layers. Consequently, the special multilayer structure design successfully endows PLA with high strength and superior toughness.

### 3.4 EMI shielding properties

Fig. 5a shows the EMI shielding curves of the composites in the X-band. CBC exhibited a stable EMI SE of approximately 15.0 dB within this frequency range. By comparison, the multilayer

samples showed a much better shielding performance, which could be continuously improved by enlarging the layer number. The maximum EMI SE of the 64L sample reached 49.8 dB. Interestingly, the multilayer composites emerged with a unique feature of frequency-selective EMI SE, which was ascribed to the Fabry–Pérot resonance effect as also existed in other layered composites.<sup>32,33</sup> The shielding peak position could be tuned by controlling the layer number. Then, the  $SE_A$  and  $SE_R$  of each sample were compared, as depicted in Fig. 5b. The  $SE_R$  values of the CBC and multilayer composites were very close to each other and no more than 5 dB, suggesting a typical absorption-dominated EMI shielding performance. In addition, the  $SE_A$  value increased with the layer number multiplied, even being nearly equal to  $SE_T$  as the layer number reached 64. To understand the EMI shielding mechanism, the electrical conduction of each composite was first tested considering its crucial role in enhancing EMI SE, as displayed in Fig. 5c. CBC exhibited a much higher  $\rho$  of  $1.2 \times 10^4 \Omega \text{ cm}$  because the MWCNT clusters confined in island-like PCL were separated by the PLA matrix. After forming the double-percolated network through multilayer structure design, MWCNT could connect well with each other to significantly decrease the  $\rho$  value. Moreover, the layer space was largely compressed as the layer number increased, making the MWCNTs connect more densely. The  $\rho$  of the 64L sample decreased to  $246 \Omega \text{ cm}$ . Apart from the much better conductivity, the structural advantage of multilayer composites was regarded as another crucial factor in achieving high EMI SE. As shown in Fig. 5d, when the incident wave contacts the surface of the multilayers, the impedance of the insulating PLA matches that of the air, resulting in a weaker wave reflection, which allows the majority of waves to penetrate the sample. Due to the presence of numerous interfaces, including the layer interfaces between PLA and ALM and the blending interfaces in individual ALM layers, the electromagnetic wave undergoes multiple reflections and continuous absorption within the sample.<sup>34</sup> This ultimately leads to an ideal EMI shielding performance of high absorption but low reflection of microwaves, which can effectively reduce a secondary electromagnetic pollution issue.

## 4 Conclusions

Herein, the PLA/ALM multilayer composites with different layer numbers were prepared by layer-assembly coextrusion, in which PLA and PCL were both continuous and MWCNTs were double percolation distributed. It was demonstrated that the PLA domains located at the layer interface could efficiently rivet the PLA and ALM layers. Thus, the nacre-like rigid-/soft-layer alternately stacked structure of multilayer composites enabled the maximum contribution to stiffness and toughness, resulting in a fracture strain of 354.4%, about quadruple that of CBC with the same compositions, while maintaining an excellent strength of above 46.0 MPa. Besides, the multilayer composites showed a special frequency-selective EMI shielding performance with an optimal SE of up to 49.8 dB. The position of the shielding peak can be adjusted by the layer number. The excellent EMI SE of the multilayer composites, mainly

contributed by absorption loss, was attributed to their high electrical conductivity and abundant interfaces capable of inducing multiple wave attenuation effects. This promising strategy opens a new window for fabricating polymeric composites with balanced mechanical properties and excellent EMI SE.

## Data availability

No primary research results, software or code have been included and no new data were generated or analysed as part of this review.

## Conflicts of interest

There are no conflicts of interest to declare.

## Acknowledgements

This work was financially supported by the National Natural Science Foundation of China (Grant No. 52373046), the Sichuan Province Distinguished Youth Fund (2022JDJQ0023), and the Opening Project of Engineering Research Center of Eco-friendly Polymeric Materials, Ministry of Education (EFP-YD2301).

## References

- 1 U. Sonchaeng, F. Iñiguez-Franco, R. Auras, S. Selke, M. Rubino and L. T. Lim, *Prog. Polym. Sci.*, 2018, **86**, 85–121.
- 2 R. M. Rasal, A. V. Janorkar and D. E. Hirt, *Prog. Polym. Sci.*, 2010, **35**, 338–356.
- 3 L. T. Lim, R. Auras and M. Rubino, *Prog. Polym. Sci.*, 2008, **33**, 820–852.
- 4 L. Yi, S. Luo, J. Shen, S. Guo and H. Sue, *ACS Sustainable Chem. Eng.*, 2017, **5**, 3063–3073.
- 5 C. Li, T. Jiang, J. Wang, H. Wu, S. Guo, X. Zhang, J. Li, J. Shen, R. Chen and X. Xiong, *ACS Appl. Mater. Interfaces*, 2017, **9**, 25818–25829.
- 6 Z. Du, G. Zhang, K. Chen, C. Zhou, X. Zhu, Y. Zhang, K. Chen, H. Y. Mi, Y. Wang, C. Liu and C. Shen, *ACS Appl. Mater. Interfaces*, 2022, **14**, 14607–14617.
- 7 Y. Wang, Z. W. Fan, H. Zhang, J. Guo, D. X. Yan, S. Wang, K. Dai and Z. M. Li, *Mater. Design*, 2021, **197**, 109222.
- 8 G. Wang, G. Zhao, S. Wang, L. Zhang and C. B. Park, *J. Mater. Chem. C*, 2018, **6**, 6847–6859.
- 9 Y. Han, J. Shi, L. Mao, Z. Wang and L. Zhang, *Ind. Eng. Chem. Res.*, 2020, **59**, 21779–21790.
- 10 M. Zhang, C. Jiang, Q. Wu, G. Zhang, F. Liang and Z. Yang, *ACS Macro Lett.*, 2022, **11**, 657–662.
- 11 Z. Jing, X. Huang, X. Liu, M. Liao, Z. Zhang and Y. Li, *RSC Adv.*, 2022, **12**, 13180–13191.
- 12 I. Navarro-Baena, V. Sessini, F. Dominici, L. Torre, J. M. Kenny and L. Peponi, *Polym. Degrad. Stab.*, 2016, **132**, 97–108.
- 13 R. Umamaheswara Rao, B. Venkatanarayana and K. N. S. Suman, *Mater. Today: Proc.*, 2019, **18**, 85–97.





- 14 S. Balali, S. M. Davachi, R. Sahraeian, B. S. Heidari, J. Seyfi and I. Hejazi, *Biomacromolecules*, 2018, **19**, 4358–4369.
- 15 B. Zhu, Y. Wang, H. Liu, J. Ying, C. Liu and C. Shen, *Compos. Sci. Technol.*, 2020, **190**, 108048.
- 16 J. N. Coleman, U. Khan, W. J. Blau and Y. K. Gun'ko, *Carbon*, 2006, **44**, 1624–1652.
- 17 J. R. Tao, D. Yang, Y. Yang, Q. M. He, B. Fei and M. Wang, *Polymer*, 2022, **252**, 124963.
- 18 Z. Xu, Y. Zhang, Z. Wang, N. Sun and H. Li, *ACS Appl. Mater. Interfaces*, 2011, **3**, 4858–4864.
- 19 Y. J. Tan, J. Li, X. H. Tang, T. N. Yue and M. Wang, *Composites, Part A*, 2020, **137**, 106088.
- 20 J. R. Tao, C. L. Luo, M. L. Huang, Y. X. Weng and M. Wang, *Composites, Part A*, 2023, **164**, 107304.
- 21 Y. Liu, H. He, G. Tian, Y. Wang, J. Gao, C. Wang, L. Xu and H. Zhang, *Compos. Sci. Technol.*, 2021, **214**, 108956.
- 22 Y. Zheng, X. Ji, M. Yin, J. Shen and S. Guo, *ACS Appl. Mater. Interfaces*, 2017, **9**, 32270–32279.
- 23 B. Zeng, L. Yang, J. Qin, Y. Zheng and S. Guo, *ACS Appl. Mater. Interfaces*, 2020, **12**, 52008–52017.
- 24 Y. Zheng, B. Zeng, L. Yang, J. Shen and S. Guo, *Ind. Eng. Chem. Res.*, 2020, **59**, 2977–2987.
- 25 G. Mayer, *Science*, 2005, **310**, 1144–1147.
- 26 Z. Yin, F. Hannard and F. Barthelat, *Science*, 2019, **364**, 1260–1263.
- 27 B. Zeng, M. Cao, J. Shen, K. Yang, Y. Zheng and S. Guo, *Polymer*, 2022, **242**, 124546.
- 28 Y. Zheng, X. Ji, Q. Wang, J. Shen and S. Guo, *RSC Adv.*, 2018, **8**, 42337–42345.
- 29 Y. Zheng, J. Qin, J. Shen and S. Guo, *J. Mater. Chem. C*, 2020, **8**, 9593.
- 30 J. Ai, B. Zeng, J. Qin, Y. Zheng and S. Guo, *Polym. Test.*, 2022, **115**, 107749.
- 31 K. Fukushima, C. Abbate, D. Tabuani, M. Gennari and G. Camino, *Polym. Degrad. Stab.*, 2009, **94**, 1646–1655.
- 32 P. Song, X. Liao, F. Zou, X. Wang, F. Liu, S. Liu and G. Li, *Compos. Commun.*, 2022, **34**, 101264.
- 33 G. Wang, X. Liao, J. Yang, W. Tang, Y. Zhang, Q. Jiang and G. Li, *Compos. Sci. Technol.*, 2019, **184**, 107847.
- 34 M. Wang, X. Tang, J. Cai, H. Wu, J. Shen and S. Guo, *Carbon*, 2021, **117**, 377–402.

